Materials Research Bulletin 101 (2018) 146–154

Contents lists available at ScienceDirect

Materials Research Bulletin

journal homepage: www.elsevier.com/locate/matresbu

Distribution and mobility of lithium in NASICON-type $Li_{1-x}Ti_{2-x}Nb_x(PO_4)_3$ ($0 \leq x \leq 0.5$) compounds

Radhouene Kahlaoui[a,b,*], Kamel Arbi[b,c], Ricardo Jimenez[b], Isabel Sobrados[b], Jesus Sanz[b], Riadh Ternane[a]

[a] Laboratoire d'Application de la Chimie aux Ressources et Substances Naturelles et à l'Environnement (LACReSNE), Université de Carthage, Faculté des Sciences de Bizerte, 7021 Zarzouna, Bizerte, Tunisia
[b] Instituto de Ciencia de Materiales de Madrid (ICMM), Consejo Superior de Investigaciónes Científicas (CSIC), Cantoblanco, 28049 Madrid, Spain
[c] Department of Materials and Environment (Microlab), Faculty of Civil Engineering & Geosciences, Delft University of Technology, The Netherlands

ARTICLE INFO

Keywords:
Structural materials
X-ray diffraction
Nuclear magnetic resonance (NMR)
Energy storage
Ionic conductivity

ABSTRACT

The NASICON-type $Li_{1-x}Ti_{2-x}Nb_x(PO_4)_3$ ($0 \leq x \leq 0.5$) has been prepared using a conventional solid-state reaction and characterized by powder X-ray (XRD), scanning electron microscopy (SEM), nuclear magnetic resonance (NMR) and impedance spectroscopy (IS). The substitution of Ti^{4+} by Nb^{5+} in $LiTi_2(PO_4)_3$ increases unit cell parameters of NASICON phases (S.G. $R\bar{3}c$). The parallel XRD and NMR analysis confirmed the formation of secondary phases besides NASICON compounds. The NMR components detected in ^{93}Nb and ^{31}P MAS-NMR spectra have been ascribed to formation of crystalline $NbPO_5$ and NASICON phases. The substitution of Ti^{4+} by Nb^{5+} produces detection of three equally spaced ^{31}P MAS-NMR $P(OTi)_{4-n}(ONb)_n$ components, whose intensity changes with the Nb content of the NASICON phase. On the other hand, the broad ^{31}P NMR band detected at ~ -130 ppm has been ascribed to the formation of an amorphous Nb phosphate that strongly affects conductivity of samples. At 355 K, total conductivity decreased from 1.2×10^{-7} S cm^{-1} (Ea = 0.49 eV) to 6.0×10^{-9} S cm^{-1} (Ea = 0.56 eV) when going from $LiTi_2(PO_4)_3$ to $Li_{0.5}Ti_{1.5}Nb_{0.5}(PO_4)_3$. This important decrease has been related to the increment of activation energy (stronger Li-network interaction); however, further studies are required to understand the deleterious effect of niobium in $Li_{1-x}Ti_{2-x}Nb_x(PO_4)_3$ series.

1. Introduction

Lithium-ion rechargeable batteries are considered as the best appropriate power source for different applications such as electric vehicles (EVs), implantable medical devices and large scale energy storage systems (ESSs). Recently, considerable research has been concentrated on Li fast ion conductors with NASICON (Na Super-Ionic Conductor) structure to be used as solid electrolyte in Li-ion batteries [1–3].

The NASICON $LiM_2(PO_4)_3$ structure can be described as $[M_2(PO_4)_3]^-$ lanterns that share vertices with contiguous units to form a three-dimensional network. $LiM_2(PO_4)_3$ (M = Ti^{4+}, Ge^{4+}) compounds, display rhombohedral symmetry (S.G. $R\bar{3}c$) [4,5], while in other compositions (M = Sn^{4+}, Zr^{4+}, Hf^{4+}), a triclinic distortion was detected at low temperature (S.G. $C\bar{1}$) [6–8]. Samples derived from the rhombohedral $LiTi_2(PO_4)_3$ phase (S.G. $R\bar{3}c$) display appropriated conductivity and chemistry stability [9,10].

The most appropriate strategy to change the Li content in NASICON compounds is the substitution of titanium by other cations [11]. The structure of $LiTi_2(PO_4)_3$ is flexible for partial substitution of Ti^{4+} with trivalent like Al^{3+}, Ga^{3+}, Sc^{3+}, Fe^{3+}, Cr^{3+}, or Y^{3+} [12–16], tetravalent- Zr^{4+} [17] and pentavalent Nb^{5+} or V^{5+} cations [18–21], giving rise to a considerable amount of derived compounds. In conduction pathways, Li cations can occupy M1 and M2 sites: in M1 sites Li is sixfold coordinated at the Wyckoff position 6b (0, 0, 0) of ternary axes, however, in M2 sites Li is tenfold coordinated at 18e (x, 0, 1/4), disposed symmetrically around three-fold axes [22].

At room temperature, the maximum reported conductivity ($\sigma_{RT} \approx 10^{-3}$ S cm^{-1}) was found in Al^{3+} [13,14] and Sc^{3+} [13,15] doped compounds. Neutron diffraction refinements of $Li_{1+x}Ti_{2-x}Al_x(PO_4)_3$ samples showed that most part of Li is located at octaheral M1 sites, but some part of Li is coordinated to four oxygens at M3 sites in M2 cavities [22]. The increment of conductivity was ascribed to formation of vacancies at M1 sites (intersection of three conduction paths). The creation of vacancies at M1 sites can also be achieved by substitution of Ti by pentavalent cations [18–20].

* Corresponding author at: Laboratoire d'Application de la Chimie aux Ressources et Substances Naturelles et à l'Environnement (LACReSNE), Université de Carthage, Faculté des Sciences de Bizerte, 7021 Zarzouna, Bizerte, Tunisia.
E-mail address: kradhouene960@gmail.com (R. Kahlaoui).

https://doi.org/10.1016/j.materresbull.2018.01.022
Received 31 May 2017; Received in revised form 9 October 2017; Accepted 17 January 2018
Available online 04 February 2018

In the present work, the NASICON-series $Li_{1-x}Ti_{2-x}Nb_x(PO_4)_3$ ($0 \le x \le 0.5$) has been investigated. Special attention has been paid to determine the amount of niobium incorporated into NASICON compounds and the formation of secondary phases. In this study, the influence of M1 vacancies on Li conductivity is investigated. XRD and MAS-NMR (^{93}Nb and ^{31}P) techniques have been used to characterize structure of formed phases, and IS and ^{7}Li MAS-NMR techniques to analyze Li^+ mobility.

2. Experimental

Compounds with the nominal composition $Li_{1-x}Ti_{2-x}Nb_x(PO_4)_3$ ($0 \le x \le 0.5$) have been synthesized by solid-state reaction. Stoichiometric amounts of high purity Li_2CO_3 (> 99%, Merck), TiO_2 (98%, Aldrich), Nb_2O_5 (99.5%, Aldrich) and $(NH_4)_2HPO_4$ (> 97%, Roth) reagents were used. These compounds were first dried at 390 K for 10 h to remove any traces of water; then mixed in an agate mortar and heated up to 1173 K for 2 h in platinum crucible [14,15] to obtain the NASICON compounds. The temperature and reaction times were chosen to minimize the formation of secondary phases. In particular, the heating at 1273 K, produced the segregation of some TiO_2 from NASICON phases. After thermal treatments, X-ray diffraction was used to check the elimination of starting reagents and formation of final compounds.

X-ray diffraction (XRD) patterns were recorded at room temperature on a Bruker D8-advance diffractometer (40 kV and 30 mA), using the 1.5406 Å Cu-Kα1 radiation. Data were collected in the 10°−110° (2θ) range with 0.02° steps of 0.5 s counting time/step. Crystalline phases were identified using the International Centre for Diffraction Data (ICDD). Le Bail technique was used to determine lattice parameters of samples. Structural refinements were performed with the $R\bar{3}c$ model (FullProf program) [23,24]. In Rietveld refinements, a pseudo-Voigt function was chosen to describe the line shape of diffraction peaks. In a first stage, scale factors, 2θ zero positions, background coefficients, line-width and peaks-shape were determined. In a second stage, positional parameters, site occupations and atom thermal factors were deduced. Agreement factors decrease considerably when the amount of Nb increases as a consequence of secondary amorphous phases formed.

NMR spectra were recorded at room temperature with an AVANCE-400 Bruker spectrometer (9.4 T magnetic field). ^{6}Li, ^{7}Li, ^{93}Nb, and ^{31}P NMR signals were recorded at 58.88, 155.45, 97.85 and 161.97 MHz frequencies; using 5.0 µs pulse lengths for ^{6}Li, 3.5 µs for ^{7}Li, 2.0 µs for ^{93}Nb, and 4.0 µs for ^{31}P signals. In Magic Angle Spinning (MAS) experiments, spectra were recorded on samples rotated at 10 kHz around an axis inclined 54°44′ with respect to the external magnetic field. The number of scans was in the range 100 − 800. The NMR shifts of components were referred to 1M LiCl, 1M $NbCl_5$ and 85% H_3PO_4 aqueous solutions. Spectra deconvolution was performed with the Winfit software package (Bruker) [25], which allowed intensity, linewidth and position of components to be deduced with a nonlinear least-square iterative program. NMR quadrupole C_Q and asymmetry η parameters were determined with trial and error procedures.

Surface and cross section images of prepared pellets were obtained with scanning electron microscopy (SEM) technique. Samples for SEM were deposited on a metallic support and coated with a gold film before observation in a JEOL 6400 electron microscope operating at 20 kV.

Electrical measurements were carried on cylindrical pellets (~6 mm in diameter and 1.5 mm in thickness), obtained by applying an uniaxial 120 MPa pressing and 12 h of sintering at 1123 K. Gold electrodes were formed from pastes deposited on the two faces of pellets. Samples were placed in a JANIS VPF 750 cryostat under vacuum atmosphere, allowing 4 L-configuration (2 probes) measurements. An automatically controlled Agilent Precision LCR E4980-A analyzer was used for frequency measurements (5 Hz–10^7 Hz). The electrical characterization was performed between 305 K and 465 K (at 10 K intervals). The spectra were analyzed using the ZView2 impedance software [26].

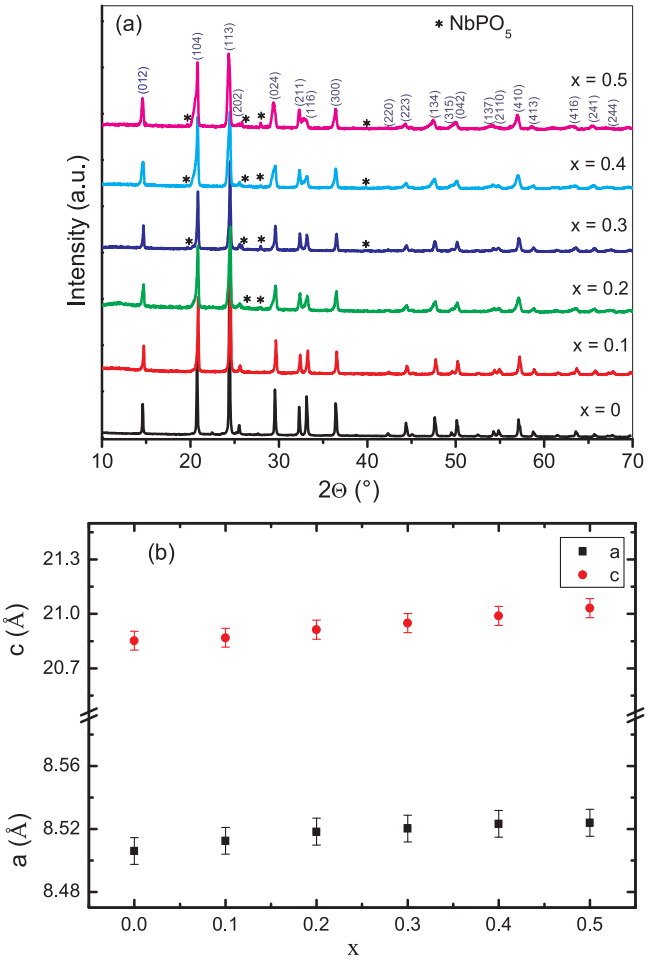

Fig. 1. (a) X-ray powder diffraction patterns and (b) dependence of unit cell parameters with composition of $Li_{1-x}Ti_{2-x}Nb_x(PO_4)_3$ samples.

3. Results and discussion

3.1. X-ray diffraction

XRD patterns of $Li_{1-x}Ti_{2-x}Nb_x(PO_4)_3$ ($0 \le x \le 0.5$) samples, recorded at room temperature, are given in Fig. 1a. In all analyzed samples, XRD patterns display peaks of rhombohedral (S.G. $R\bar{3}c$) NASICON phases (JCDPS No. 035–0754). For $x \ge 0.2$, small XRD peaks corresponding to $NbPO_5$ (JCDPS No. 073–1609) coexist with those of NASICON compounds. The dependence of NASICON *a* and *c* parameters with the Nb content is given in Fig. 1b. A linear variation of unit cell parameters (Vegard's law) was observed with the substitution of Ti^{4+} by Nb^{5+} ions (r_{Ti4+} = 0.605 Å, r_{Nb5+} = 0.640 Å) [27]. However, small departures from linearity, observed in Nb-rich samples, indicate that not all Nb is incorporated in NASICON compounds (Fig. 1b).

In Rietveld refinements, the rhombohedral $LiTi_2(PO_4)_3$ structure was used as starting model. Structural analysis revealed that only M1 (6*b*) sites were occupied by Li atoms (see Fig. 2). Observed, calculated, and difference XRD patterns of $Li_{0.9}Ti_{1.9}Nb_{0.1}(PO_4)_3$ and $Li_{0.7}Ti_{1.7}Nb_{0.3}(PO_4)_3$ are depicted as examples in Fig. 3a and b. In Li-rich ($x \le 0.1$) samples, reliability R_p factors ranged between 7.5–8.5%, R_{wp} between 9.3–10.4%, R_F between 2.0–2.8% and χ^2 between 1.2–1.6. In Nb rich samples ($x > 0.2$), figures of merit increased considerably (R_p from 10.1 to 17.7%, R_{wp} from 11.2 to 18.9%, R_F from 2.6 to 7.1%). The consideration of the $NbPO_5$ phase improved refinements; however, figures of merit remained below those of Li-rich samples (Fig. 3b). In all analyzed series, the amount of $NbPO_5$ phase do not exceed 5%. The linewidth of XRD peaks increase along the series, indicating that the

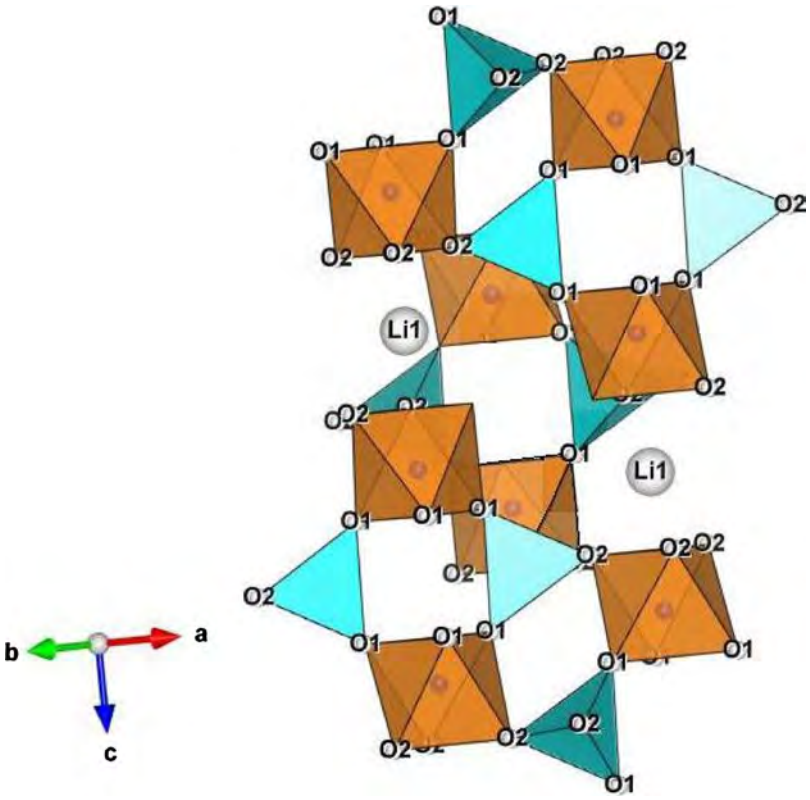

Fig. 2. Schematic view of the $Li_{0.9}Ti_{1.9}Nb_{0.1}(PO_4)_3$ crystal structure, illustrating P (blue) and Ti (orange-brown) polyhedra. In this figure, lithium M1 sites (Li1) are also indicated.

NASICON crystallite particles size decrease from 70.4 to 52.0 nm when the amount of Nb increases.

Atom positions, thermal factors and sites occupancy of the NASICON $Li_{0.9}Ti_{1.9}Nb_{0.1}(PO_4)_3$ sample are depicted in Table 1. Structural refinement of NASICON phases leads to acceptable Ti,Nb–O and P–O distances: Ti,Nb–O distances vary between 1.89(1)–1.96(5) and P–O distances between 1.52(2)–1.56(8) Å. In Ti,Nb octahedra two detected distances indicate a shift of Ti inside octahedra, that disappears as Nb content increases (Table 2). In conduction channels, Li1–O_2 distances vary between 2.27(3)–2.33(1) Å. At room temperature, thermal B_{Li} factors increased from 1.40(3) to 3.25(5) with the Li content, suggesting a higher mobility of lithium in Li-rich samples.

3.2. NMR

^{93}Nb MAS-NMR

^{93}Nb (I = 9/2) MAS-NMR spectra of $Li_{1-x}Ti_{2-x}Nb_x(PO_4)_3$ ($0 \le x \le 0.5$) are formed by nine transitions modulated by sample spinning sidebands (asterisks of Fig. 4). In ^{93}Nb MAS-NMR spectra satellite transitions display very low intensity, making difficult the estimation of quadrupolar interactions [28,29]. This impedes the correction of second-order quadrupolar effects on chemical shift values of components. Based on these considerations, only relative position of central ^{93}Nb components will be discussed here.

The study of niobio-phosphates showed the shift towards more negative values of the central ^{93}Nb NMR component as the number of phosphate groups increase in $Nb(OP)_x(ONb)_{6-x}$ associations [30]. According to this work, the dominant component at −1625 ppm has been ascribed to octahedral niobium of NASICON phases, sharing oxygens with six PO_4 tetrahedra. The small component detected near −932 ppm has been ascribed to the secondary $NbPO_5$ phase, where Nb cations share oxygens with four PO_4 tetrahedra and two NbO_6 octahedra. Finally, NbO_6 signals ascribed to niobate oxides, with chemical shift values near −1000 ppm were not detected here.

To reproduce experimental profiles of samples, a broad component at ~ −1615 ppm was considered, that was ascribed to the formation of a disordered phase with similar environments of NASICON phases. In the case of the sample x = 0.1, the central transition displays a bigger asymmetry towards more negative positions, that has often be associated with structural disordering [28]. On the other hand, the −2100 ppm component, ascribed to NbO_8 environments by I. Yu. Pinus et al. [18], has not been detected in our samples.

^{31}P MAS-NMR

^{31}P (I = 1/2) MAS-NMR spectra of the $Li_{1-x}Ti_{2-x}Nb_x(PO_4)_3$ ($0 \le x \le 0.5$) samples are depicted in Fig. 5. $LiTi_2(PO_4)_3$ displays a single component at −27.6 ppm, ascribed to $P(OTi)_4$ environments [14]. This component becomes broadened as a consequence of small distortions produced in PO_4 tetrahedra of Nb doped samples.

In ^{31}P MAS-NMR spectra of $Li_{1-x}Ti_{2-x}Nb_x(PO_4)_3$ samples, the substitution of Ti^{4+} by Nb^{5+} induces the polarization of oxygen atoms, shifting P components towards more negative values. The opposite trend was detected when Ti^{4+} ions are substituted by trivalent cations [14,15]. This has permitted the assignment of detected components to $P(OTi)_4$, $P(OTi)_3(ONb)_1$ and $P(OTi)_2(ONb)_2$ environments in $Li_{1-x}Ti_{2-x}Nb_x(PO_4)_3$ samples (lines labeled (0), (1) and (2) in Fig. 5). The deconvolution of ^{31}P MAS-NMR spectra of $Li_{0.7}Ti_{1.7}Nb_{0.3}(PO_4)_3$ and $Li_{0.5}Ti_{1.5}Nb_{0.5}(PO_4)_3$ phases are given in the top of Fig. 5.

The quantitative analysis of ^{31}P MAS-NMR spectra allowed the determination of Nb/Ti ratios of NASICON phases, with the expression [15,31] :

$$\frac{Nb^{5+}}{Ti^{4+}} = \frac{2I_2 + I_1}{4I_0 + 3I_1 + 2I_2} = \frac{x}{2 - x}$$

where I_n (n = 0, 1, 2) stands for the intensity of bands associated with (2-n)Ti.(n)Nb environments. From Nb/Ti values, the relative amounts of Nb (x) and Ti (2-x) were deduced (Table 3). In general, it is observed that the amount of Nb incorporated in NASICON phases (x^{NMR}) is lower than nominal values (x), increasing this difference with the Nb content.

As Nb increases, a small component at ~ −24 ppm and a broad band at −31 ppm were detected (Fig. 5). The first component was

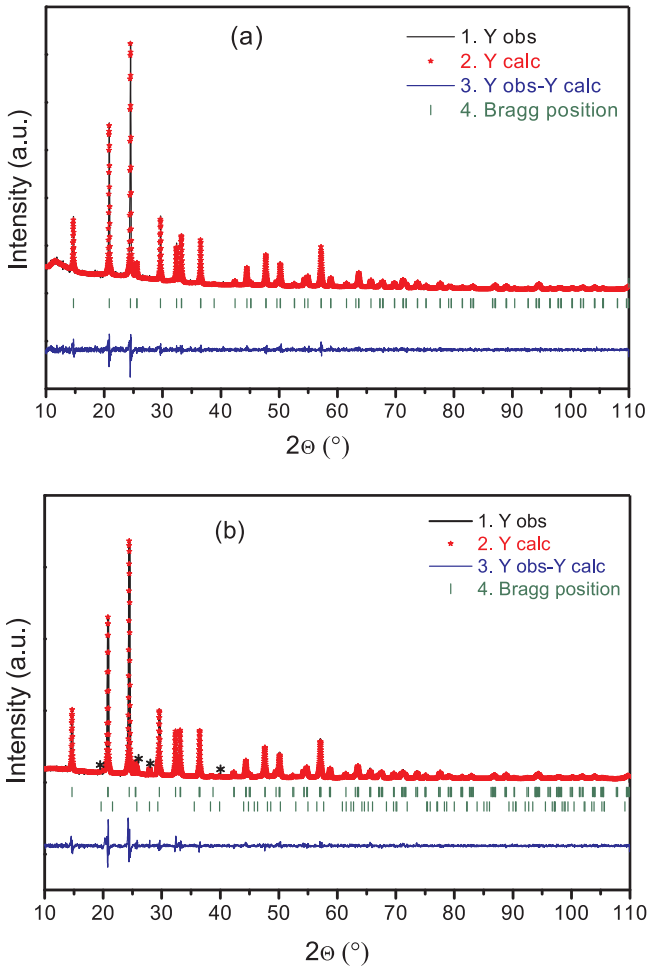

Fig. 3. RT Rietveld refinement of (a) $Li_{0.9}Ti_{1.9}Nb_{0.1}(PO_4)_3$ and (b) $Li_{0.7}Ti_{1.7}Nb_{0.3}(PO_4)_3$ patterns. In this figure, profiles calculated with the R$\bar{3}$c model were compared with experimental ones. Asterisks denote peaks of secondary $NbPO_5$ phase.

Table 1
Structural parameters deduced from the Rietveld refinement of $Li_{0.9}Ti_{1.9}Nb_{0.1}(PO_4)_3$.

Atom	Wyckoff position	x	y	z	B	Occupancy
Li1 (M1)	6b	0	0	0	1.89 (9)	0.95 (3)
Ti	12c	0	0	0.140 (9)	0.25 (5)	1.86 (5)
Nb	12c	0	0	0.140 (9)	0.25 (5)	0.13 (2)
P	18e	0.288 (8)	0	1/4	0.48 (9)	3
O_1	36f	0.187 (5)	0.991 (4)	0.188 (4)	1.22 (7)	6
O_2	36f	0.190 (5)	0.165 (4)	0.081 (5)	0.86 (5)	6

a = 8.512 (2) Å, c = 20.867 (3) Å, V = 1309.4 (1) Å^3, R_B = 2.09%, R_F = 2.77%, R_p = 7.51%, R_{WP} = 9.35%, χ^2 = 1.16.

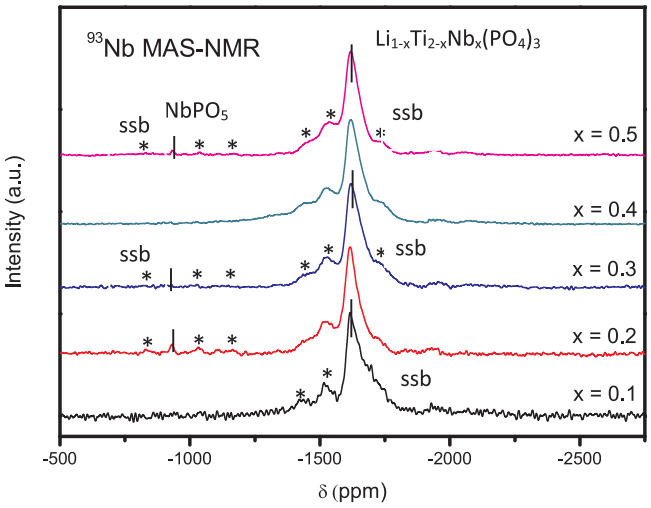

Fig. 4. ^{93}Nb MAS-NMR central components of $Li_{1-x}Ti_{2-x}Nb_x(PO_4)_3$ samples spectra. Central components of NASICON and $NbPO_5$ phases are denoted with vertical line-sspinning side bands (ssb) of both compounds are denoted with asterisks. The separation between ssb maxima corresponds to the sample spinning rate (c/s).

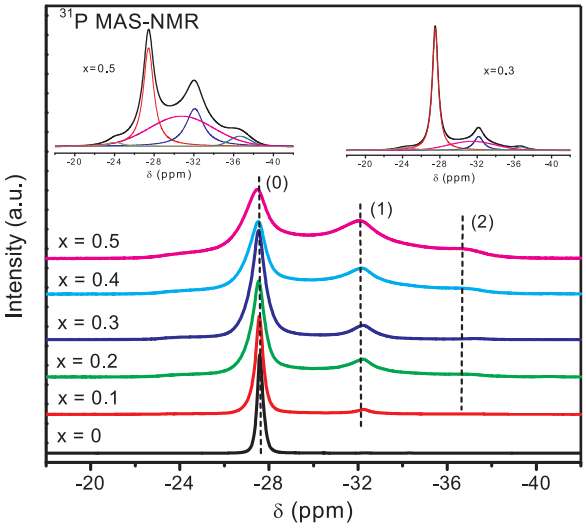

Fig. 5. ^{31}P MAS-NMR central components of $Li_{1-x}Ti_{2-x}Nb_x(PO_4)_3$ spectra. The deconvolution of x = 0.3 and x = 0.5 spectra are given in the top of the figure.

ascribed to $NbPO_5$ phases and the broad one to amorphous phosphates. The presence of an amorphous phase, with compositions near NASICON phases, suggests that temperature used in preparations was not sufficiently high for NASICON formation; however, the segregation of part of TiO_2 from NASICON's compounds, prevented the use of thermal treatments above 1173 K [18].

In summary, ^{31}P MAS-NMR spectra indicate the existence of two main phases: (1) equally spaced components correspond to crystalline

Table 2
Interatomic Li1 − O, Ti,Nb − O and P − O distances (Å) deduced from structural refinements of $Li_{1-x}Ti_{2-x}Nb_x(PO_4)_3$ samples. Percentage (%) of NASICON and $NbPO_5$ crystalline phase are also depicted*.

x	Li1(M1) − O_2	Ti,Nb − O_1	Ti,Nb − O_2	P − O_1	P − O_2	(%) NASICON phase	(%) $NbPO_5$ phase
0	2.27 (3)	1.89 (1)	1.96 (5)	1.54 (8)	1.53 (2)	100	—
0.1	2.30 (1)	1.89 (7)	1.95 (4)	1.54 (2)	1.53 (2)	100	—
0.2	2.30 (7)	1.90 (4)	1.94 (7)	1.53 (2)	1.54 (1)	98.92 (1)	1.08 (1)
0.3	2.31 (3)	1.91 (2)	1.93 (1)	1.53 (4)	1.55 (1)	97.91 (1)	2.09 (1)
0.4	2.32 (2)	1.92 (6)	1.93 (3)	1.52 (6)	1.55 (4)	96.45 (1)	3.55 (1)
0.5	2.33 (1)	1.93 (2)	1.92 (9)	1.52 (2)	1.56 (8)	94.66 (1)	5.34 (1)

*The presence of amorphous phases cannot be detected by XRD.

Table 3
Chemical shift δ_{iso}(ppm), quadrupole constant C_Q (kHz), asymmetry parameter η (dimensionless), full width at half maximum FWHM (kHz) and percentage (%) of species deduced from ^{7}Li and ^{31}P MAS-NMR spectra of $Li_{1-x}Ti_{2-x}Nb_x(PO_4)_3$ samples.

x	x^{NMR}	C_Q	δ(Li)	η	FWHM	δ(P(OTi)$_4$)	δ(P(OTi)$_3$ (ONb)$_1$)	δ(P(OTi)$_2$ (ONb)$_2$)	δ(Amorphous phase)	(%)* Amorphous
0	0	43	1.28	0	0.06	−27.61	–	–	–	–
0.1	0.04	44	1.25	0	0.07	−27.55	−32.25	−36.98	−30.00	8.68
0.2	0.08	46	1.30	0	0.07	−27.52	−32.20	−36.97	−30.02	9.89
0.3	0.12	47	1.33	0	0.08	−27.50	−32.17	−36.68	−31.44	22.82
0.4	0.22	49	1.35	0	0.09	−27.48	−32.15	−36.53	−31.01	37.24
0.5	0.26	49	1.37	0	0.09	−27.43	−32.08	−36.61	−31.02	40.74

*The presence of amorphous phases reduces the relative amount of crystalline NASICON in the samples.

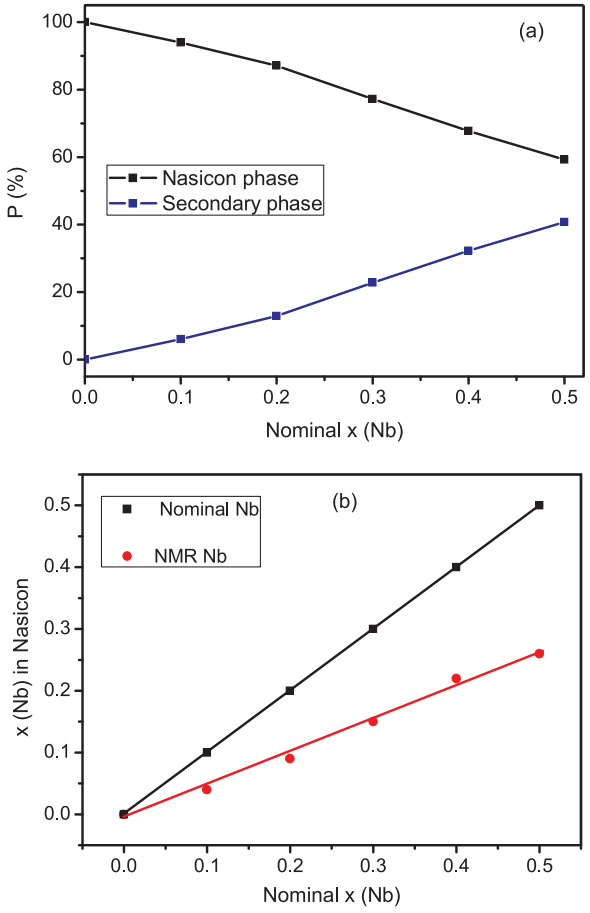

Fig. 6. (a) Phosphorus (%) in NASICON and secondary phases vs. Nb nominal contents. (b) Niobium (x) content deduced from ^{31}P MAS-NMR spectra in NASICON phases.

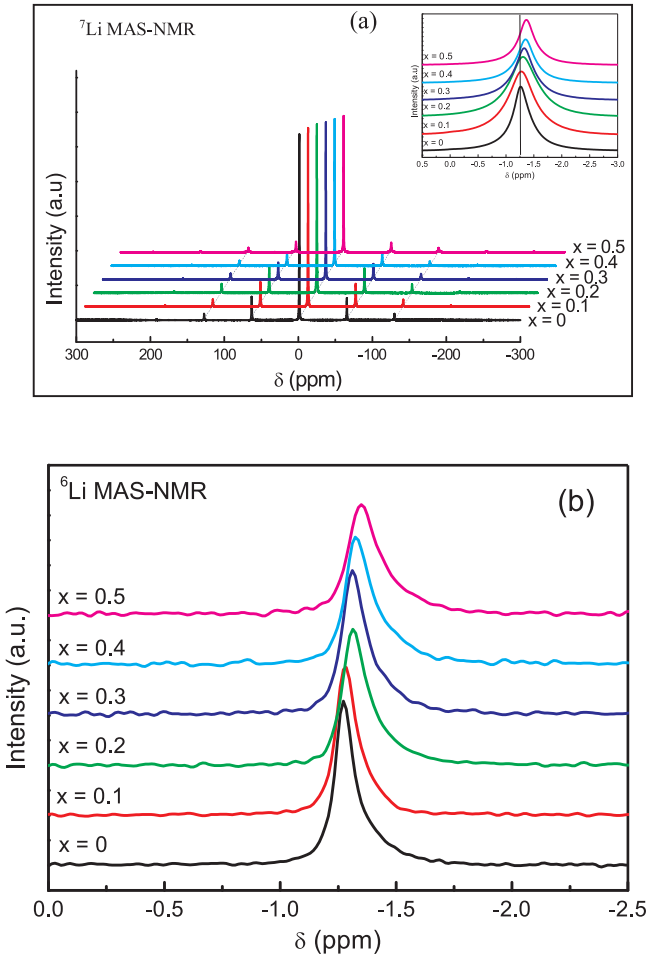

Fig. 7. (a) ^{7}Li and (b) ^{6}Li MAS-NMR spectra of $Li_{1-x}Ti_{2-x}Nb_x(PO_4)_3$ samples.

NASICON and (2) the broad band correspond to disordered phosphates. The quantitative analysis of the ^{31}P MAS-NMR spectrum of the sample x = 0.5 shows that the amount of phosphorous incorporated in NASICON and secondary phases are respectively 59% and 41% (Fig. 6a). According to this, the niobium incorporated in NASICON phases, deduced from ^{31}P MAS-NMR spectra (Table 3), is always lower than nominal one (Fig. 6b), increasing differences with the Nb content.

^{6,7}Li MAS-NMR

^{7}Li and ^{6}Li MAS-NMR spectra of the $Li_{1-x}Ti_{2-x}Nb_x(PO_4)_3$ ($0 \le x \le 0.5$) samples are shown in Fig. 7a and b. The ^{7}Li (I = 3/2) spectra are formed by the central ± 1/2 ↔ ± 1/2 and lateral ± 3/2 ↔ ± 1/2 transitions, modulated by equally spaced spinning sidebands (Fig. 7a). In ^{6}Li MAS-NMR (I = 1) spectra, only a single component results from 0 ↔ ± 1 transitions (Fig. 7b). The deconvolution of NMR central components permitted an estimation of chemical shift values (δ_{iso}) and line-widths (FWHM) of components. Quadrupolar constants (C_Q and η) deduced from ^{7}Li MAS-NMR spectra are given in Table 3.

In $LiTi_2(PO_4)_3$, M1 sites are mainly occupied by Li^+ (η values near zero). The incorporation of Nb reduces the Li content, increasing the amount of M1 vacant sites. According to this, quadrupole C_Q values do not change significantly and asymmetry η remains always zero, indicating that Li ions remain at M1 sites. From the analysis of the central linewidth (FWHM), it was deduced that mobility of lithium is higher in Li-rich than in Li-poor samples. As the Nb content increases, the central component shifts towards more negative values and increases its linewidth, from 60 to 90 Hz, suggesting the presence of several non-resolved components (inset of Fig. 7a and Table 3). This observation could again be associated with formation of a disordered phase.

3.3. SEM study

In Fig. 8a, c, e, the fresh fracture image of ceramic pellets with nominal Nb composition x = 0.1, 0.3, 0.5 can be found. For the same

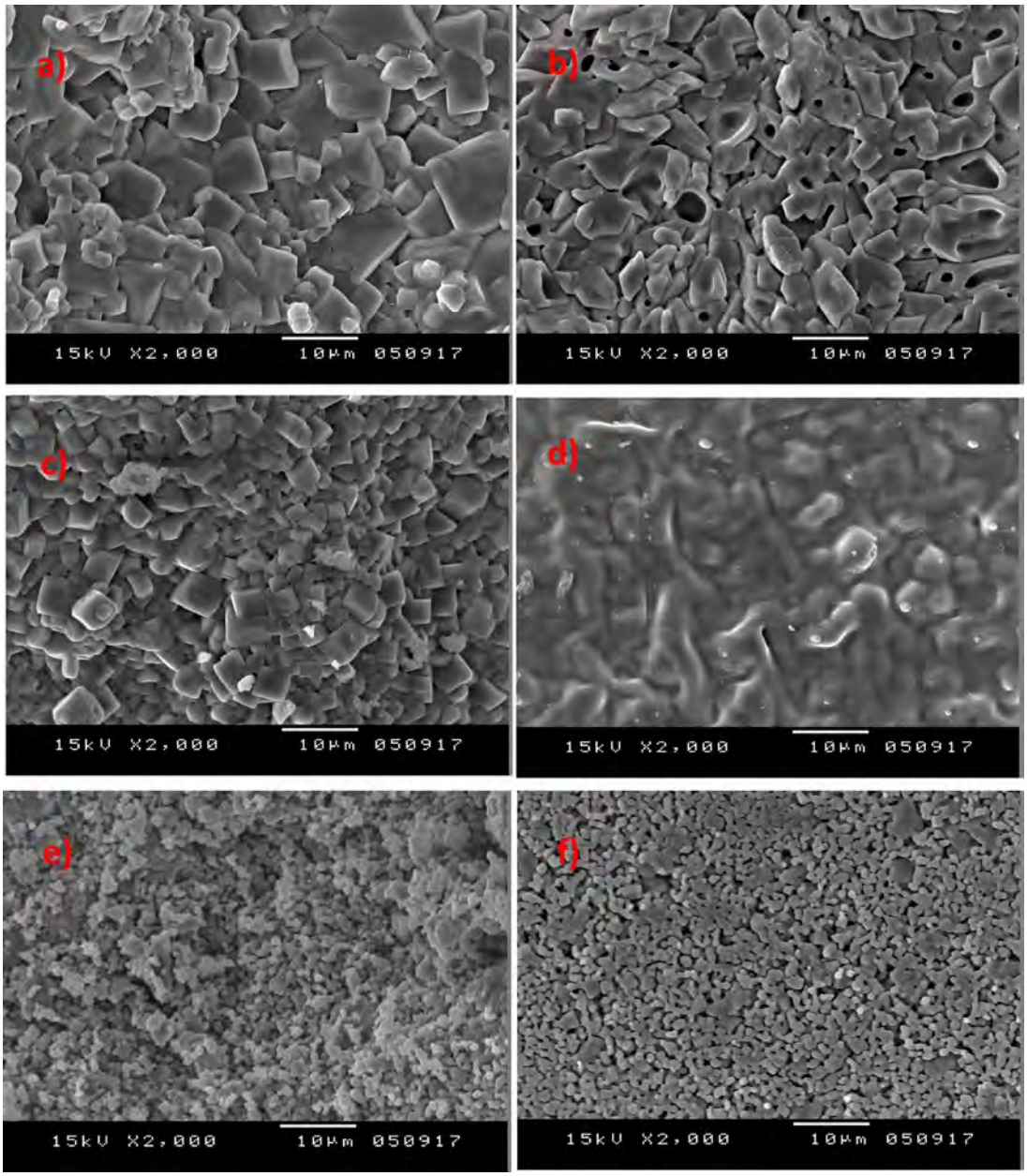

Fig. 8. SEM micrographs of $Li_{1-x}Ti_{2-x}Nb_x(PO_4)_3$ samples with nominal x = 0.1, 0.3, 0.5 compositions. Images a, c and e correspond to fresh fracture images and b, d and f to surface of ceramic pellets.

samples the SEM image of the surface of the pellets can be found in Fig. 8b, d, f. In sample x = 0.1, the mean size of particles ranges from 2 to 10 µm. Particles exhibit well defined faces in fresh fracture image surface but more rounded contacts among particles in the surface of the ceramic. Small porosity is observed in Fig. 8b, where observed pores are detected in the interior of agglomerates. From these images it can be inferred that the NASICON particles are well connected trough tiny contacts.

In the fresh fracture image of ceramics with nominal Nb content x = 0.3 (Fig. 8c), analyzed particles display a more homogeneous distribution centered around 5 µm size, with almost no pores. In the ceramic surface image, porosity has disappeared and rounded particles are interconnected trough thick glassy boundaries. The formation of an important quantity of glassy phase around the NASICON particles can explain the broad band detected in ^{31}P MAS-NMR spectra. A large variety of P environments explains the absence of well defined spinning sidebands in the corresponding NMR pattern. In this sample, the amorphous phase seems to surround crystalline NASICON nuclei, showing a different contrast in surface and nuclei of particles (core-shell structures).

In agreement with broadened XRD peaks detected in sample x = 0.5, the size of particles has considerably decreased to 1 µm, as can be observed in the corresponding fresh fracture SEM image (Fig. 8e). Moreover particles can be grouped it two different types, displaying different gray intensity, that agree with relative amounts of two detected phosphates. The surface image of the pellet showed a homogeneous particle size distribution with an important increase of porosity with respect intermediate compositions. Small rounded particles are again connected trough glassy boundaries. In this case, the surface/volume ratio of NASICON particles increased as a consequence of the particles size decrease. The particles size lowering explain the crystallinity loss detected in XRD patterns. Density of samples was determined with the Archimedes method, decreasing from 93.5 to 80.7 g cm^{-3} as the Nb content increased (Table 4).

Table 4
Apparent, theoretical and relative density of $Li_{1-x}Ti_{2-x}Nb_x(PO_4)_3$ samples.

x	Apparent density ($g\,cm^{-3}$)	Theoretical density ($g\,cm^{-3}$)	Relative density (%)
0	2.76	2.95	93.5
0.1	2.58	2.97	86.8
0.2	2.53	2.99	84.6
0.3	2.52	3.02	83.4
0.4	2.50	3.03	82.5
0.5	2.47	3.06	80.7

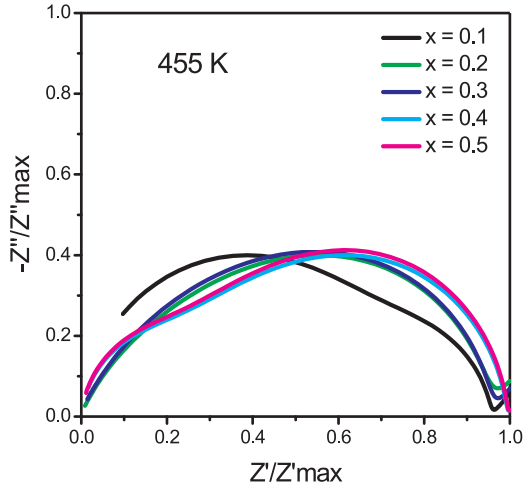

Fig. 9. Nyquist plots of $Li_{1-x}Ti_{2-x}Nb_x(PO_4)_3$ samples recorded at 455 K.

3.4. Electrical properties

Li mobility was investigated with Impedance Spectroscopy in the NASICON $Li_{1-x}Ti_{2-x}$ $Nb_x(PO_4)_3$ series. In these samples, Nyquist plots are constituted by two semicircles or a single broad semicircle, being difficult the resolution of bulk and grain boundary contributions. Normalized complex impedance plots measured at 455 K are given in Fig. 9. In this plot it was observed that impedance diagrams for x = 0.1, 0.4 and 0.5 are similar. In these samples, typical "bulk" and grain boundary responses, with different time constants, could be resolved. In x = 0.2 and 0.3 samples, a distorted semicircle was associated with the presence of non-resolved "grain boundary" and "bulk" responses. At 455 K, the study of the electrode contribution (incipient spike, see Fig. 9), showed Li blocking at Au electrode, indicating that Li conduction is preponderant in analyzed samples.

The plot of the real part of permittivity vs. frequency (not shown), displays a large permittivity increment that separates bulk and grain boundary responses. In Fig. 10a and b, the frequency dependence of conductivity, measured at various temperatures, is given for $LiTi_2(PO_4)_3$ and $Li_{0.7}Ti_{1.7}Nb_{0.3}(PO_4)_3$ samples. Derivative plots were used to determine dc. conductivity values [32]. In $LiTi_2(PO_4)_3$, "bulk" and grain boundary contributions were differentiated (Fig. 10a); however, in $Li_{0.7}Ti_{1.7}Nb_{0.3}(PO_4)_3$ sample, the plateau of the "bulk" response was not resolved (Fig. 10b). The lack of resolution has been ascribed to compositional heterogeneities that increases grain boundary contributions and hinders the detection of the bulk contribution. In the analysis of the SEM images, a thick vitreous phase surround NASICON particles. The relative large thickness of this layer increases the convolution between the impedance of the "bulk" response of NASICON particles and the grain boundary of thick amorphous layers.

The dc conductivity obeys the Arrhenius equation

$$\sigma_{dc} x\, T = A_0 \exp\left(\frac{-Ea}{k_B T}\right)$$

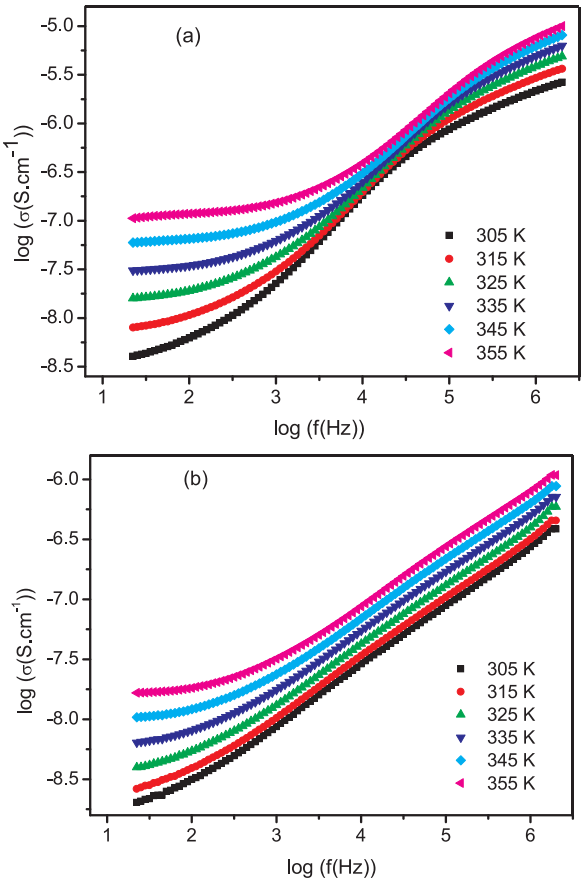

Fig. 10. Real conductivity vs. frequency in (a) $LiTi_2(PO_4)_3$ and (b) $Li_{0.7}Ti_{1.7}Nb_{0.3}(PO_4)_3$ samples.

where σ_{dc} is the dc-conductivity, A_0 stands for the pre-exponential factor, E_a is the activation energy for the Li^+ ion migration, T is the absolute temperature (K) and k_B is the Boltzmann constant. In the case of x = 0 and 0.1 samples, the bulk conductivity at 355 K could be determined. In particular, $\sigma_b = 2.3 \times 10^{-5}\,S\,cm^{-1}$ was measured in x = 0 (0.38 eV), and decreased to $2.3 \times 10^{-7}\,S.cm^{-1}$ in x = 0.1 sample (0.62 eV). For x = 0.2 and 0.3, bulk conductivity could not be resolved from total conductivity. In x = 0.4 and 0.5 samples, "bulk" conductivity decreased to 3.2×10^{-8} (0.58 eV) to finally decrease to 1.9×10^{-8} (0.61 eV) (Table 5). The rather good separation of the conductivity time constant for the "bulk" and grain boundary contributions in x = 0.4 and 0.5 samples is related to the microstructure observed in Fig. 8e. For this sample the amorphous shells of particles are thin allowing the separation of the corresponding time constants.

Li mobility has been shown to depend on relative occupation of two crystallographic sites of NASICON compounds. In $LiTi_2(PO_4)_3$, Li^+ occupy most of M1 sites favoring the onset of correlated motions [12,33,34]. In $Li_{1+x}Ti_{2-x}Al_x(PO_4)$, the increment of the Li content

Table 5
Total ionic conductivity (σ_t) and activation energy (E_a) at 355 K of $Li_{1-x}Ti_{2-x}Nb_x(PO_4)_3$ samples. Bulk ion conductivity (σ_{bulk}) and activation energy (Ea) are only given for some compositions.

x	σ_t ($S\,cm^{-1}$)	E_a (eV)	σ_{bulk} ($S\,cm^{-1}$)	E_a (eV)
0	1.2×10^{-7}	0.49	2.34×10^{-5}	0.38
0.1	4.5×10^{-8}	0.51	2.32×10^{-7}	0.62
0.2	3.5×10^{-8}	0.52	—	—
0.3	1.53×10^{-8}	0.53	—	—
0.4	1.09×10^{-8}	0.55	3.16×10^{-8}	0.58
0.5	6.02×10^{-9}	0.56	1.91×10^{-8}	0.61

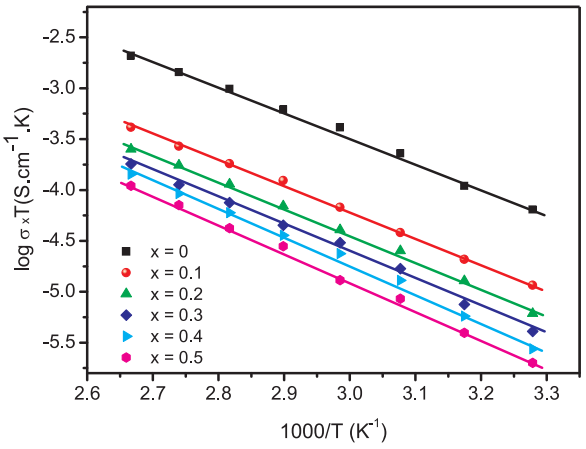

Fig. 11. Arrhenius plots of total dc-conductivity in $Li_{1-x}Ti_{2-x}Nb_x(PO_4)_3$ samples.

increased the repulsion between Li^+ ions at M1 and M3 sites, favoring the occupation of M3 sites. In these samples, small Li-network interactions and allocation of vacancy at M1 sites favored the delocalization of Li along … M1-M3-M1-M3... channels. In $Li_{1-x}Ti_{2-x}Nb_x(PO_4)_3$ series, the incorporation of Nb^{5+} increased the amount of vacancy at M1 sites, what should increase Li hoping between partial occupied M1 sites. The Li hoping probability should be given by

$$F_{LiV} = C_{Li}x\, C_V/C_{Li} + C_V$$

where C_{Li} and C_V are Li and vacancy occupation of M1 sites. The increment of conductivity was not observed experimentally indicating that not only M1 vacancy affect Li mobility.

To explain the decrease on conductivity with Nb substitution, it must be assumed that creation of vacancy at M1 sites reduces conductivity. This effect is contrary to what produced by Ti^{4+} for Al^{3+} substitution, where vacancy M1 sites favored Li hoping. The incorporation of small amounts of Nb produces a strong reduction of bulk conductivity that must be associated with an increment of migration energy. Another possible effect associated with Nb incorporation could be the vacancy ordering, that as reported previously hinder Li motions [11]. A discussion of possible causes that decrease Li mobility, requires a deeper study of Li-network interactions with DFT simulation techniques [35].

The inverse temperature dependence of the total σ_{dc} conductivity is given in Fig. 11. The values of total dc-conductivities and activation energies, measured at, 355 K, are given in Table 5. It is observed that total conductivity decreases with Nb doping. The $LiTi_2(PO_4)_3$ end member exhibits the best total conductivity, (1.2×10^{-7} S cm^{-1}), and the lowest activation energy (0.49 eV). In the case of $Li_{0.9}Ti_{1.9}Nb_{0.1}(PO_4)_3$, total conductivity decrease to 4.5×10^{-8} S cm^{-1} and activation energy increased to 0.51 eV. This agrees with values reported in literature [18,33,34]. For remaining samples the total conductivity decreased again till 6.02×10^{-9} S cm^{-1} and activation energy increased to 0.56 eV.

The increment of the Nb content favors also the formation of an amorphous secondary phase (see Table 3). The increment of the convolution between the "bulk" and grain boundary conductivity time constants contributions can be explained by a broadening of disordered shells that surround NASICON particles. However, activation energy for total d.c. conductivity is lower than "bulk" one. This result is not usual in Li-NASICON ceramics and should deserve further study. It is possible that, the large quantity of amorphous phases in x = 0.4 and 0.5 be evenly distributed in ceramics. The study of Li ion conductivity in amorphous phases deserved further investigation with alternative composite models [36].

4. Conclusions

NASICON $Li_{1-x}Ti_{2-x}Nb_x(PO_4)_3$ ($0 \le x \le 0.5$) samples were synthesized by solid-state reaction and characterized with XRD, NMR and IS techniques. In prepared samples, crystalline and amorphous materials were detected, indicating that incorporation of Nb to the NASICON structure (S.G. R $\bar{3}$c) is not easy at 1173 K. In Nb rich samples, besides NASICON phases, an small amount of crystalline $NbPO_5$ phases was detected.

The substitution of Ti^{4+} by Nb^{5+} in NASICON phases, increases unit cell parameters but decreases "bulk" Li conductivity from 2.3×10^{-5} to 1.9×10^{-8} S cm^{-1} at 355 K. In the temperature range investigated, activation energy increases from 0.38 to 0.62 eV with Nb content.

$^{6/7}$Li MAS-NMR spectra showed the presence of Li atoms at M1 sites of NASICON phases. Li mobility decreased when the niobium increased and Li content decreased, suggesting that the decrease detected on "bulk" d.c conductivity must be attributed to stronger Li-network interactions (increment of activation energy) in Nb doped samples. The formation of a disordered (amorphous) phase in quite large quantity reduces the volume fraction of crystalline NASICON in the samples and its distribution seems to be responsible for the evolution of the total resistance detected in prepared ceramics.

Acknowledgements

R.K. would like to thank the Tunisian Ministry of Higher Education and Scientific Research for financial support. This work was funded by Spanish MINECOMAT2013-46452-C4-2R and MATERYENER3-CAM (S2013/MIT-2753) projects.

References

[1] J.B. Goodenough, H.Y.P. Hong, J.A. Kafalas, Mater. Res. Bull. 11 (1976) 203.
[2] K. Nagata, T. Nanno, J. Power Sources 174 (2007) 832.
[3] H. Aono, E. Sugimoto, Y. Sadaoka, N. Imanaka, G.-Y. Adachi, Chem. Lett. 10 (1990) 1825.
[4] M. Alami, R. Brochu, J.L. Soubeyroux, P. Graverau, G. Le Flem, P.J. Hagenmuller, J. Solid State Chem. 90 (1991) 185.
[5] M.A. Paris, A. Martinez-Juarez, J.M. Rojo, J. Sanz, J. Phys. Condens. Matter. 8 (1996) 5355.
[6] E. Morin, J. Angenault, J.C. Couturier, M. Quarton, H. He, J. Klinowski, Eur. J. Solid State Inorg. Chem. 34 (1997) 947.
[7] M. Catti, S. Stramare, R. Ibberson, Solid State Ionics 123 (1999) 173.
[8] E.R. Losilla, M.A.G. Aranda, M. Martinez-Lara, S. Bruque, Chem. Mat. 9 (1997) 1678.
[9] X. Xu, Z. Wen, X. Yang, J. Zhang, Z. Gu, Solid State Ionics 177 (2006) 2611.
[10] N. Anantharamulu, K. Koteswara Rao, G. Rambabu, B. Vijaya Kumar, V. Radha, M. Vithal, J. Mater. Sci. 46 (2011) 2821.
[11] R. Kahlaoui, K. Arbi, R. Jimenez, I. Sobrados, M. Mehnaoui, J. Sanz, R. Ternane, Ionics 23 (2017) 837.
[12] K. Arbi, M. Hoelzel, A. Kuhn, F. García-Alvarado, J. Sanz, Inorg. Chem. 52 (2013) 9290.
[13] H. Aono, E. Sugimoto, Y. Sadaoka, N. Imanaka, G.-Y. Adachi, J. Electrochem. Soc. 137 (1990) 1023.
[14] K. Arbi, S. Mandal, J.M. Rojo, J. Sanz, Chem. Mater. 14 (2002) 1091.
[15] R. Kahlaoui, K. Arbi, I. Sobrados, R. Jimenez, J. Sanz, Riadh Ternane, Inorg. Chem. 56 (2017) 1216.
[16] F.E. Mouahid, M. Zahir, P. Maldonado-Manso, S. Bruque, E.R. Losilla, M.A.G. Aranda, A. Rivera, C. Leon, J. Santamaria, J. Mater. Chem. 11 (2001) 3258.
[17] K. Arbi, M. Tabellout, J. Sanz, Solid State Ionics 180 (2010) 1613.
[18] I.Yu. Pinus, A.V. Khoroshilov, K.S. Gavrichev, V.P. Tarasov, A.B. Yaroslavtsev, Solid State Ionics 212 (2012) 112.
[19] M. Forsyth, S. Wong, K.N. Nairin, A.S. Best, P.J. Newman, D.R. MacFarlane, Solid State Ionics 124 (1999) 213.
[20] X. Shang, H. Nemori, S. Mitsuoka, Y. Mastuda, Y. Takeda, O. Yamamoto, N. Imanishi, Solid State Ionics 297 (2016) 43.
[21] A.S. Best, P.J. Newman, D.R. MacFarlane, K.M. Nairin, S. Wong, M. Forsyth, Solid State Ionics 126 (1999) 191.
[22] A. Aatiq, M. Menetrier, L. Croguennec, E. Suard, C. Delmas, J. Mater. Chem. 12 (2002) 2971.
[23] Rodriguez-Carvajal, J. Phys. B 192 (1993) 55.
[24] H.M. Rietveld, J. Appl. Crystallogr. 2 (1969) 65.
[25] Bruker WINFIT program, Bruker Rep. 140 (1994) 43.
[26] D. Johnson, Zview2 2.8 (2003).
[27] R.D. Shannon, Acta Crystallogr. Sect. A: Cryst. Phys. Diffr. Theor. Gen. Crystallogr. A32 (1976) 757.

[28] O.B. Lapina, D.F. Khabibulin, K.V. Romanenko, Z.H. Gan, M.G. Zuev, V.N. Krasil'nikov, V.E. Fedorov, Solid State Nucl. Magn. Reson. 28 (2005) 204.
[29] L.S. Du, R.W. Schurko, N. Kim, C.P. Grey, J. Phys. Chem. A 106 (2002) 7876.
[30] A. Flambard, L. Montaigne, L. Delevoye, S. Steuernagel, Solid State NMR 32 (2007) 34.
[31] P. Maldonado-Manso, M.C. Martín-Sedeño, S. Bruque, J. Sanz, E.R. Losilla, Solid State Ionics 178 (2007) 43.
[32] W. Bucheli, R. Jiménez, J. Sanz, Solid State Ionics 227 (2012) 113.
[33] K. Takada, M. Tansho, I. Yanase, T. Inada, A. Kajiyama, M. Kouguchi, S. Kondo, M. Watanabe, Solid State Ionics 139 (2001) 247.
[34] N.V. Kosova, E.T. Devyatkina, A.P. Stepanov, A.L. Buzlukov, Ionics 14 (2008) 303.
[35] V. Diez-Gomez, K. Arbi, J. Sanz, J. Am. Chem. Soc. 138 (2016) 9479.
[36] R. Jimenez, Solid State Ionics 90 (1996) 233.